Tunable focus and multiple plasmonic bottles from the superposition of half Pearcey plasmons

JunXi Zhang, YanRu Chen, Zhang Ruan, ZiEn Feng, ZeHong Liang, HeChong Chen, GuangHui Wang,* and DongMei Deng†

School of Information and Optoelectronic Science and Engineering, South China Normal University, Guangzhou 510006, China and Provincial Key Laboratory of Nanophotonic Functional Materials and Devices, South China Normal University, Guangzhou 510631, China

(Received 4 December 2023; revised 10 March 2024; accepted 15 May 2024; published 3 June 2024)

In this paper we utilize the half Pearcey function as a means to describe a surface plasmon, the half Pearcey plasmon. The abrupt autofocusing and self-healing properties from the superposition of the half Pearcey plasmon are observed and discussed. The tunable focal intensity covers three orders of magnitude and the autofocusing property can be maintained with the potential well. Additionally, with the π phase offset, we construct multiple plasmonic bottles with the chirp factor; both the bottle structure and propagating direction are adjustable. The focusing properties of the plasmon under the chirp depend on the spatial spectrum separation, resulting in the construction of plasmonic bottles with different positions and sizes. The validity of our results is confirmed by finite-difference time-domain numerical simulations. Our findings may provide potential for spectral enhancement, nanoscale plasmonic devices, and plasmonic trapping.

DOI: 10.1103/PhysRevA.109.063501

I. INTRODUCTION

In recent years, nanotechnology and nanomanipulation methods have achieved significant advancements and progress, among which the study of the surface plasmon polariton (SPP) has garnered widespread attention [1–3]. The SPP is an electromagnetic wave that occurs at the metal-electrolyte interface, caused by the oscillation of free electrons, whose intensity decays exponentially in the normal direction of the interface. This wave is small in scale, confining energy at the interface and breaking the limitations of optical diffraction. Up to now, the exploration on the SPP has greatly contributed to the development of nanomaterials [4], acoustic phonons [5], and metasurfaces [6] and it has potential in particle control [7,8], high-sensitivity sensors [9], and waveguides [10]. Salandrino and Christodoulides proposed and theoretically elaborated on a new type of plasmon based on the nondiffracting self-accelerating Airy solution [11], which propagates with properties of self-acceleration and self-healing. Since then, various plasmons have been demonstrated due to their distinctive propagation properties and practical applications, such as the Bessel-like plasmon [12], the Airy-Talbot plasmon [13], and the Olver plasmon [14].

Ring *et al.* creatively proposed the Pearcey beam inspired by the Pearcey function of catastrophe theory [15,16]. Also, the recently proposed Pearcey plasmon [17] exhibits comparable propagation characteristics, including dual self-bending, self-focusing, and self-healing abilities. Several novel beams originating from the Pearcey function have been proposed, expanding the family of Pearcey beams [18–20]. Among these, the half Pearcey beam extends from the Pearcey beam [21], with unique characteristics. A significant portion of these Pearcey beams are used to construct optical tweezers or bottles for particle capture, rotation, and manipulation [22,23]. However, for particles that are small on the surface, the plasmonic tweezers and bottles show better performance [24]. Wei *et al.* produced plasmonic void arrays based on a cosine-Gaussian plasmon beam [25]. In Ref. [26], a plasmonic bottle with controlled shape based on the self-accelerating plasmon was generated. So far, the Pearcey plasmon has not been used to generate plasmonic bottles for particle capture in the field of nanomanipulation.

In this article we utilize the half Pearcey function as the initial field of the SPP to investigate its captivating properties. The highly tunable autofocusing ability and the plasmonic bottles with potential in nanotrapping are obtained by phase superposition of 0 and π, respectively. Regarding the 0 phase offset, our observation indicates its strong self-focusing capability, and it has higher and more concentrated focal intensity than the Pearcey plasmon. In addition, we validate its self-healing ability by introducing a one-dimensional (1D) potential well, and the intensity modulation capable of three orders of magnitude can be modulated by the decay factor and width of the potential well. As for the π phase offset, the SPP constructed on existing trajectories with the chirp factors features a plane structure resembling a bottle profile. Also, we observe that the number of chirp factors is not equal to the number of foci. Under the modulation of the chirp factor, the low-frequency and high-frequency components of the plasmonic bottle will each have a distinct focus at different distances. In contrast to the methods used to generate plasmonic bottles in previous studies [25,26], the bottles generated with the superposition of the half Pearcey plasmon and the chirp factor in this article do not require specially structured coupling devices. The number, size, position, and

*wanggh@scnu.edu.cn
†dengdongmei@m.scnu.edu.cn

propagation direction of the bottles can be modulated conveniently and flexibly by regulating the initial field or filtering out a specific spatial spectrum. Finally, we perform numerical simulations using the finite-difference time-domain (FDTD) method, which yields results consistent with the theoretical results.

The structure of the paper is as follows. The theoretical model for exciting the SPP is introduced in detail in Sec. II. Then we discuss the propagation properties of the half Pearcey plasmon and the superposition of two half Pearcey plasmons with different phase offsets, respectively. Here we obtain a tunable self-focusing as well as multiple plasmonic bottles in Sec. III. In Sec. IV we utilize FDTD numerical simulation to realize the generation of the superposition of the half Pearcey plasmon. We summarize in Sec. V.

II. THEORETICAL MODEL

We solve the scalar Helmholtz equation governing the electric field in the paraxial approximation, at the interface between a metallic substrate and a dielectric medium, with dielectric constants ε_d and ε_m, respectively,

$$\nabla^2 E_y + k_0^2 \varepsilon_d E_y = 0, \tag{1}$$

where ∇^2 is the Laplace operator and k_0 is the wave number in vacuum. The SPP wave is excited at the x-z plane and propagates along the z axis, exponentially decaying away from metallic substrate along the y axis. According to the electric fields of the transverse magnetic wave, we separate the variables and obtain the expressions

$$\begin{aligned} E_y(x,y,z) &= \psi(x,z)\exp(ik_z z)\exp(-\alpha_d y), \\ E_z(x,y,z) &= -\frac{i\alpha_d}{k_z}\psi(x,z)\exp(ik_z z)\exp(-\alpha_d y), \end{aligned} \tag{2}$$

where k_z represents the wave vector in the z direction, which is linked to the dispersion relations of the SPP: $k_z = k_0\sqrt{\varepsilon_d\varepsilon_m/(\varepsilon_d+\varepsilon_m)}$ and $\alpha_d^2 = k_z^2 - k_0^2\varepsilon_d$. Additionally, the evolution of the transverse wave profile is determined by the potential-free linear Schrödinger equation

$$i\frac{\partial\psi(x,z)}{\partial z} + \frac{1}{2k_z}\frac{\partial^2\psi(x,z)}{\partial x^2} = 0, \tag{3}$$

where $\psi(x,z)$ represents the complex envelope amplitude of the incident wave. Consequently, the remaining transverse electric-field component can be derived as

$$E_x(x,y,z) = -\frac{\alpha_d\exp(ik_z z)\exp(-\alpha_d y)}{2\left(k_0^2\varepsilon_d+\alpha_d{}^2\right)}\frac{\partial\psi(x,z)}{\partial x}. \tag{4}$$

We explore the distinctive propagation characteristics of the SPP with various combinations of the half Pearcey functions. The Pearcey function is defined by an infinite integral [16]

$$\mathrm{Pe}(X,Y) = \int_{-\infty}^{+\infty} ds\exp[i(s^4 + s^2 Y + sX)], \tag{5}$$

where X and Y are dimensionless. We set the Pearcey function in the initial field as $\mathrm{Pe}(\frac{x}{w_0},\frac{y}{w_0})$ in physical space, where w_0 is a scalar representing the wave waist size. Since the y component of the electric field of the SPP is a swift field, we only consider the intensity distribution in the $y=0$ plane. The Pearcey function can be decomposed into two functions within one coordinate: $\int_0^{+\infty} ds\exp[i(s^4+\frac{x}{w_0}s^2)]$ and $\int_{-\infty}^{0} ds\exp[i(s^4+\frac{x}{w_0}s^2)]$. Obviously, since the integrand is an even function, the two prior integrations are equivalent, either of which can be called a half Pearcey (HP) function $\mathrm{Pe}^{\mathrm{half}}(\frac{x}{w_0},0)$. Next we introduce a decay factor $a>0$ to ensure the inclusion of an infinite SPP tail, guaranteeing the physical implementation of this wave. The initial input can be formulated as follows:

$$\psi(x,0) = \mathrm{Pe}^{\mathrm{half}}\left(\frac{x}{w_0},0\right)\exp\left(-a\frac{x^2}{w_0^2}\right). \tag{6}$$

To ensure the convergence of the integrals, we use a contour rotation as a means of numerical simulation [15]. In the dielectric region, we obtain the full vector expression of the electric field related to the surface plasmon

$$\begin{aligned} E_d = \frac{1}{\varepsilon_d}\Bigg[&\left(\hat{\mathrm{y}} - \frac{\mathrm{i}\alpha_d}{\sqrt{k_0^2\varepsilon_d+\alpha_d^2}}\hat{\mathrm{z}}\right)\psi(x,z) \\ &- \hat{\mathrm{x}}\frac{\alpha_d}{2\left(k_0^2\varepsilon_d+\alpha_d^2\right)}\frac{\partial\psi(x,z)}{\partial x}\Bigg] \\ &\times\exp\left(\mathrm{iz}\sqrt{k_0^2\varepsilon_d+\alpha_d^2}\right)\exp(-\alpha_d y), \end{aligned} \tag{7}$$

where $\hat{\mathrm{x}}$, $\hat{\mathrm{y}}$, and $\hat{\mathrm{z}}$ denote the unit coordinate vectors. The intensity distribution and propagation trajectory of the plasmon can be obtained via Eq. (7).

III. DISCUSSION

The HP plasmon in our research propagates at the interface between the silver substrate and the vacuum. We choose silver because it demonstrates lower loss in the visible spectrum than that of other noble metals, such as gold [27]. The permittivity of the silver substrate in the low-energy region can be described using the Drude-Sommerfeld free-electron model $\varepsilon_r(\omega) = \varepsilon_\infty - \frac{\omega_p^2}{\omega^2+i\omega\Gamma}$ [28]. By means of the split-step Fourier algorithm method [29], we calculate the theoretical trajectory of the HP plasmon. In our analysis, we take the scale $w_0 = 600$ nm and the wavelength $\lambda = 632.8$ nm. As depicted in Fig. 1(a), the HP plasmon autofocuses as it propagates in the z direction. It then inverts and is reconstructed under reverse acceleration, with opposite intensity distributions at autofocusing distance $Z_e = 2k_z w_0^2$, which corresponds to the Pearcey beam [15]. Meanwhile, the transverse intensity distribution upon propagation of the HP plasmon only varies in scale, indicating that the HP plasmon retains the property of being form invariant [17]. Figure 1(b) illustrates the intensity curve of the HP plasmon at different propagation distances z_n. To further investigate the unique propagation properties of the HP plasmon, we superpose two symmetrical half Pearcey functions with scaling factors w_0 and $-w_0$. Specifically, for the case of 0 phase offset, the initial input can be

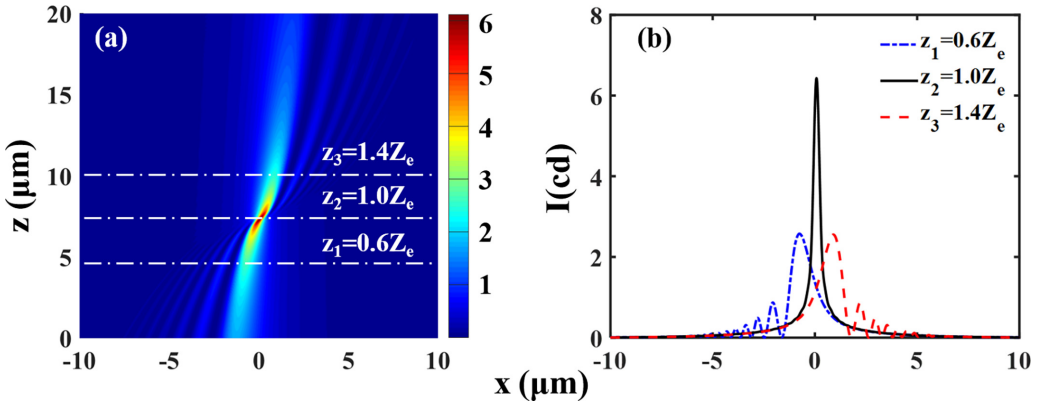

FIG. 1. (a) Intensity distribution of the HP plasmon with $a = 1/250$ in the x-z plane when $y = 0$. (b) Cross-section strength curve of the HP plasmon propagating different distances z_n. Here cd denotes candela.

derived:

$$\psi(x,0) = \left[\mathrm{Pe}^{\mathrm{half}}\left(\frac{x}{w_0},0\right) + \mathrm{Pe}^{\mathrm{half}}\left(-\frac{x}{w_0},0\right)\right] \times \exp\left(-a\frac{x^2}{w_0^2}\right). \tag{8}$$

By substituting the simulated solution $\psi(x,z)$ obtained via the split-step Fourier algorithm into Eq. (7), we can clearly describe the propagation profile of the superposition of the half Pearcey (SHP) plasmon at the $y = 0$ interface. As depicted in Fig. 2, the intensity distribution of the SHP plasmon can be interpreted as constructive interference between two HP plasmons, resulting in a more rapid increase in focal intensity. Notably, according to Fig. 2(b i), the maximum intensity is nearly 11 times higher than that in the initial field. This surge in intensity results from the lateral acceleration of the HP plasmons prior to interference, wherein energy conveyed by waves rushes towards the focal point in an accelerated manner. Furthermore, a large portion of the energy comes from the sidelobes, which gradually converge and overlap at the focal point during propagation, until they reappear after autofocusing. It is worth emphasizing that both the number of sidelobes and the focal intensity can be controlled through the decay factor a, as illustrated in Fig. 2(b i). The focal intensity

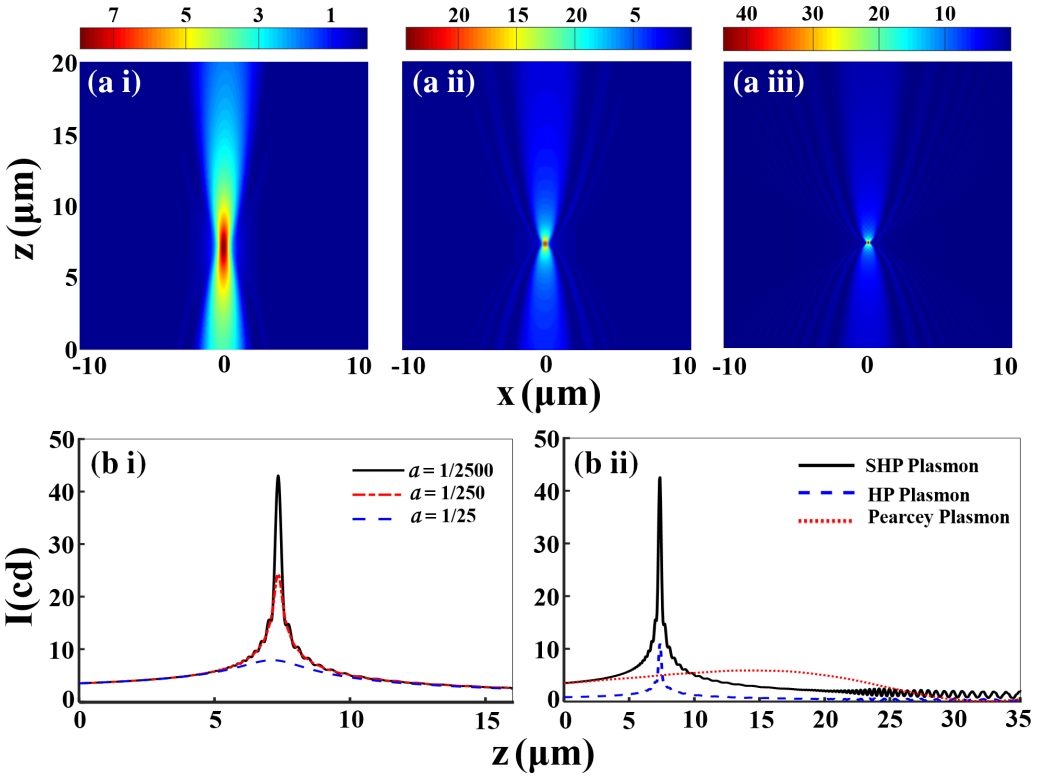

FIG. 2. (a) Intensity distributions of the SHP plasmon with different decay factors a: (a i) $a = 1/25$, (a ii) $a = 1/250$, and (a iii) $a = 1/2500$. (b i) Maximum intensity curves of the SHP plasmon in the z direction with different decay factors a. (b ii) Comparison of the maximum intensity plots of the SHP plasmon, the HP plasmon, and the Pearcey plasmon propagating in the z direction with $a = 1/2500$.

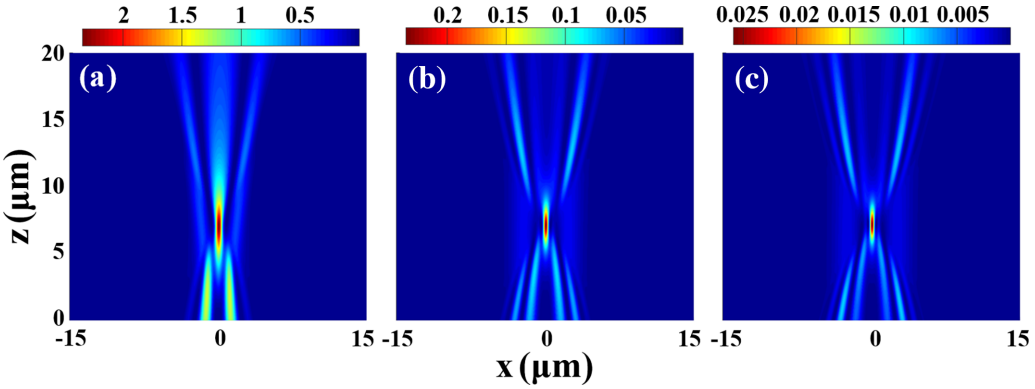

FIG. 3. Intensity distributions of the SHP plasmon with different widths γ of the 1D Gaussian soft well: (a) $\gamma = 1$ μm, (b) $\gamma = 3$ μm, and (c) $\gamma = 6$ μm.

diminishes with an increase in the decay factor, primarily due to the inhibition of energy carried by the sidelobes. Figure 2(b ii) presents the intensity curve of the SHP plasmon during propagation, allowing for a comparison of its characteristics with the Pearcey plasmon and the HP plasmon. Clearly, the focal intensity of the SHP plasmon is significantly higher and more concentrated than the Pearcey plasmon.

The self-healing feature permits the SPP to reconstruct itself after being disturbed by dents or protrusions on the metal surface. To further explore the self-healing ability of the SHP plasmon, we introduce a 1D Gaussian soft-well function as an absorption obstacle placed at the $z = 0$ plane, defined as

$$W(x) = 1 - \exp\left(-\frac{x^2}{\gamma^2}\right), \tag{9}$$

where γ is the width of the Gaussian soft well. Figure 3 displays the intensity profile affected by different widths of the soft well, with $a = 1/25$. Apparently, the energy from the sidelobes converges into the absorption obstacle region and the mainlobe reconstructs the focus. By referring to the position and the intensity of the maxima, we note that the increasing width of the well only weakens the latter, while the former is almost unchanged. These findings demonstrate that expanding the width of the soft well significantly enhances the adjustable range and flexibility of the focal intensity. Taking Fig. 2(b i) into account, the adjustable intensity covers three orders of magnitude and theoretically even higher.

Except for the phase offset of 0, we propose another SPP by superposing the HP plasmon with the π phase offset, namely, the modified-SHP plasmon. Figure 4 shows the propagation images of the modified-SHP plasmon when the decay factor a is taken as $1/250$. In contrast to the single autofocusing SPP, the initial field of the modified-SHP plasmon can be formulated as

$$\psi(x, 0) = \left[\mathrm{Pe}^{\mathrm{half}}\left(\frac{x}{w_0}, 0\right) - \mathrm{Pe}^{\mathrm{half}}\left(-\frac{x}{w_0}, 0\right)\right] \times \exp\left(-a\frac{x^2}{w_0^2}\right). \tag{10}$$

Figure 4(a) shows that the modified-SHP plasmon consists of two mainlobes. As it propagates, the modified-SHP plasmon spontaneously converges into a focus before the two lobes

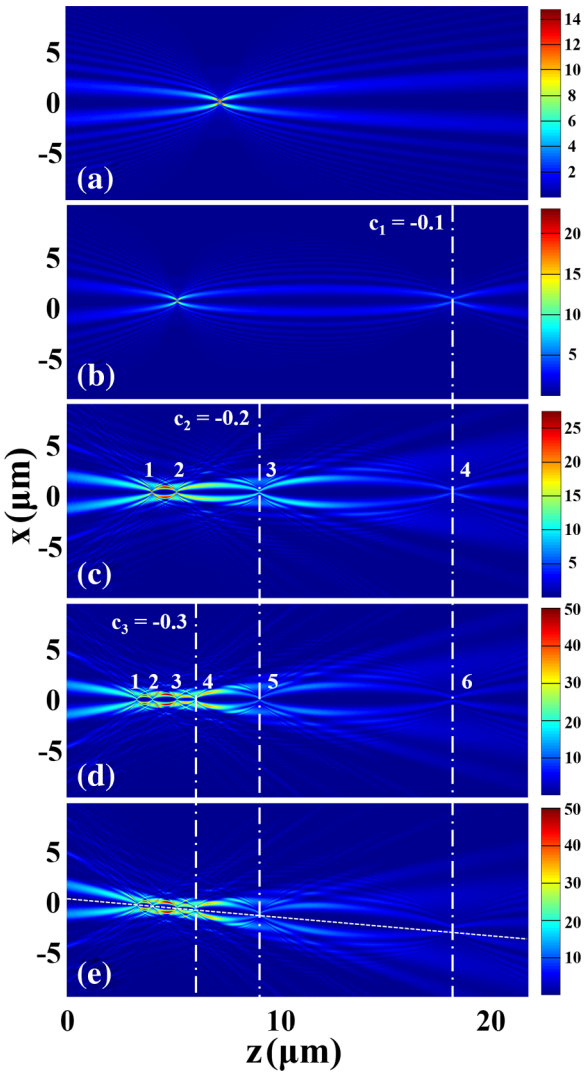

FIG. 4. Propagation of the modified-SHP plasmon with different quantities of the chirp factor c_n and the dislocation factor l, with $a = 1/2500$. The white vertical dash-dotted lines mark the foci controlled by the chirp factors, with $c_1 = -0.1$, $c_2 = -0.2$, $c_3 = -0.3$, (a) without the chirp factor, (b) with c_1, (c) with c_1 and c_2, and (d) and (e) with c_1, c_2, and c_3. In (e) the dislocation factor l is taken as -1. The dashed line in (e) serves as a guide to the eye.

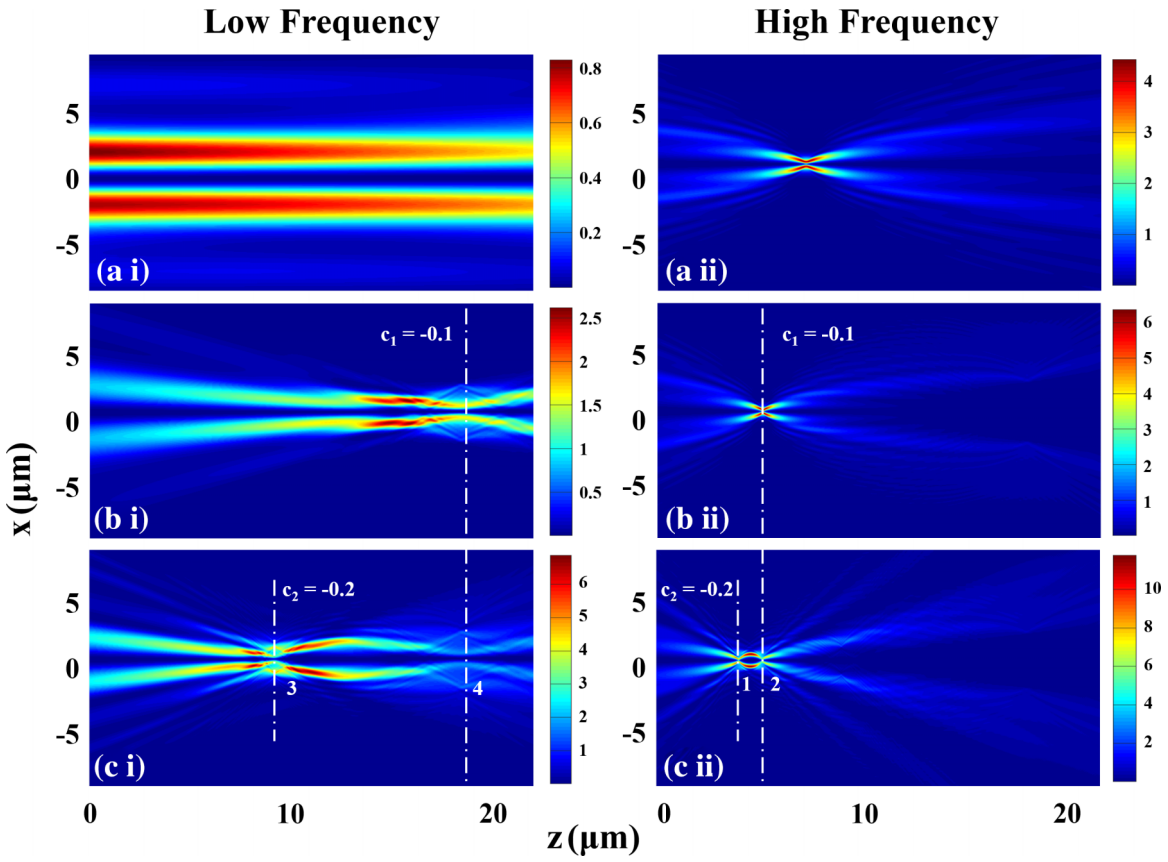

FIG. 5. Low-frequency part and high-frequency part of the modified-SHP plasmon under the influence of different chirp factors after filtering out part of the k_x spectrum. (a) Separation of the spatial spectrum from Fig. 4(a). (b) Modulation effect of chirp factor c_1 added on the low- and high-frequency parts independently, corresponding to Fig. 4(b). (c) Modulation effect of chirp factors c_1 and c_2 added on the low- and high-frequency parts independently, corresponding to Fig. 4(c). Here the white vertical dash-dotted lines mark the foci controlled by the chirp factors. The figures are obtained by filtering (a i)–(c i) the high-frequency part and (a ii)–(c ii) another frequency domain.

accelerate in symmetric directions. For the bottle-shaped intensity distribution, the target particles will be trapped in the interior of the bottle by the gradient force, which provides a theoretical model for trapping particles on the surface [30]. To construct a two-dimensional plasmonic bottle, we introduce a quadratic weak chirp factor that enables secondary focusing without any grating structures [31]. In addition, we introduce a dislocation factor l to flexibly control the position of the bottle and the propagating direction of the modified-SHP plasmon. The initial expression of the modified-SHP plasmon can be rewritten as

$$\psi(x,0) = \left[\mathrm{Pe}^{\mathrm{half}}\left(\frac{x}{w_0},0\right) - \mathrm{Pe}^{\mathrm{half}}\left(-\frac{x}{w_0},0\right)\right] \times \exp\left(-a\frac{x^2}{w_0^2}\right)\exp\left(-i\frac{lx}{w_0}\right)C(x), \tag{11}$$

where l is the dislocation factor used to alter the off-axis angle and $C(x)$ is the quadratic chirp expression, which can be represented as

$$C(x) = \sum_n^N \exp\left(-ic_n\frac{x^2}{w_0^2}\right), \tag{12}$$

where c_n is the chirp factor. The quadratic chirp behaves like a lens, causing an additional focusing of the beam, and it shares similarities with the SPP. The 1D chirp factor is equivalent to passing the initial field of the SPP through a cylindrical lens, resulting in an extra focus. The focal length can be determined as $\frac{k_z w_0^2}{2c_n}$ [32]. Here we take the modified-SHP plasmon in Fig. 4(b) as an example, as it is expected to converge again, forming a plasmonic bottle. Figures 4(b)–4(d) showcase the modified-SHP plasmon regulated by the chirp factors with different quantities and values. As expected, the SPP modulated by the chirp factor exhibits multifocusing behavior. The low-energy region surrounded by the high-intensity profile forms the plasmonic bottles, resembling the aforementioned light bottles. In addition, a comparison between Figs. 4(d) and 4(e) reveals that the dislocation factor $l = -1$ results in the modified-SHP plasmon propagating off-axis at a tunable angle, greatly improving the regulation flexibility. However, the focal length is unaffected while the focal points experience transverse displacement, further indicating that the foci through the dash-dotted line in the figures are only controllable under the chirp factors. Also, it is deduced that the dislocation factor will stretch the bottle shape. Nevertheless, if there is more than one chirp factor, we notice the number

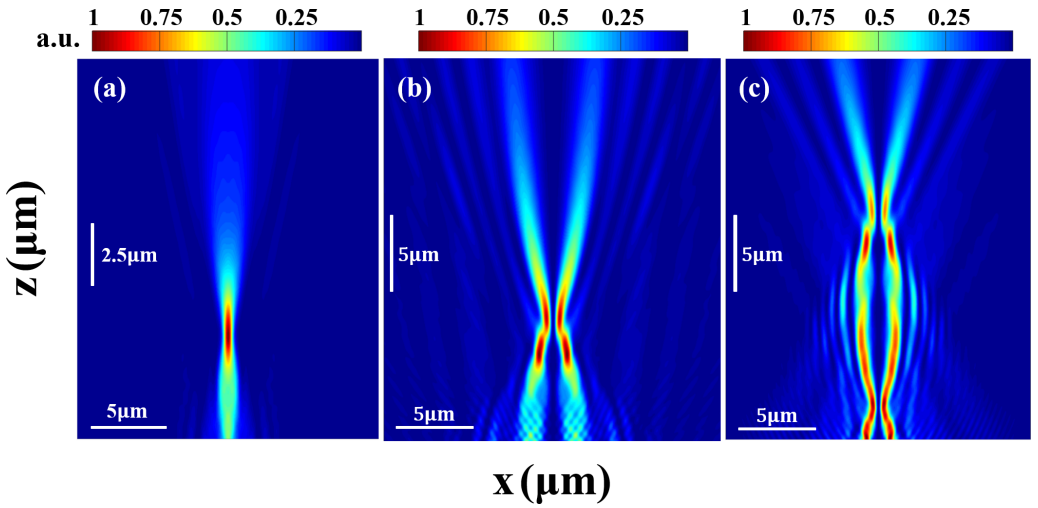

FIG. 6. Intensity distribution in FDTD numerical simulations corresponding to (a) Fig. 2(a i), (b) Fig. 4(a), and (c) Fig. 4(b) for (a) the SHP plasmon, (b) the modified-SHP plasmon, and (c) the modified-SHP plasmon with chirp factor $c = -0.1$.

of chirp factors is not equal to the number of foci. With the introduction of chirp factors, the positions of foci generated are not only at the focal length $\frac{k_z w_0^2}{2c_n}$ of the chirp, but also at shorter distances than the original autofocusing distance Z_e. For instance, in Fig. 4(c), focal points 3 and 4 result from the convergence of the modified-SHP plasmon by chirp factors c_2 and c_1, respectively, while focal points 1 and 2 are obtained by shifting the original self-focusing focus forward by different distances. The modified-SHP plasmon without the chirp factor can be divided into plane waves of different spatial frequencies. We divide the initial field into two equal-energy parts of the frequency spectrum to ensure the energy present in the high-frequency part and the low-frequency part contributes equivalently to the intensity distribution of the modified-SHP plasmon. In particular, the boundary between the low-frequency part and the high-frequency part for equal energy is set to 2.5 μm^{-1}. The propagation trajectories of the high-frequency and low-frequency parts of the modified-SHP plasmon obtained by spatial frequency domain filtering are shown in Fig. 5. Figure 5(a) showcases the low-frequency part and the high-frequency part of the modified-SHP plasmon without the chirp factor. It is obvious that the high-frequency part gradually aggregates in intensity and undergoes self-focusing during propagation, while the low-frequency part is not related to it. The results indicate that the property of self-focusing is generated by the high-frequency part. Subsequently, the quadratic chirp factor is actually equal to a lens, and we introduce the chirp factor modulation on the two frequency parts independently. As shown in Figs. 5(b) and 5(c), when the chirp factor c_n acting as a lens is introduced, the low-frequency part focuses at the focal length of the chirp factor. Simultaneously, the position of the autofocusing point generated by the high-frequency part changes due to the chirp factor, which can be derived as $\frac{Z_e}{4|c_n|+1} = \frac{2k_z w_0^2}{4|c_n|+1}$ from the lens imaging formula. Therefore, the increase in the number of foci as well as bottles can be attributed to the self-focusing property of the modified-SHP plasmon. The positions of focal points 1–4 in Fig. 4(c) are consistent with those in Fig. 5(c). When introducing n ($n = 1, 2, 3, \ldots$) chirp factors, the low-frequency part generates n focal points and the high-frequency part also focuses at n positions due to the difference in focal lengths, leading to a total of $2n - 1$ bottles. This implies we can achieve more foci with fewer chirp factors and the generated multiple plasmonic bottles of different sizes can accommodate more particle sizes. In addition, the exact position of each focal point can be calculated for precise control. These findings provide rich inspiration for the capture or confinement of nanoscale particles on the plane [8].

IV. FDTD NUMERICAL SIMULATION

In order to further verify our theoretical results, we utilize FDTD numerical simulations to confirm the characteristics of the superposition of the HP plasmon. Numerous schemes for generating the SPP have been proposed [33–35]. Considering the complexity involved in the phase spectrum of the HP plasmon and the generation device, we use periodic gratings [36] to compensate for the momentum of the incident beam and excite the plasmon at the interface between the silver substrate and the vacuum. The incident beam, carrying phase information, is directed normal to the periodic grating with $\lambda = 632$ nm and $w_0 = 600$ nm. The period of the grating in the propagation direction is λ, and the silver layer has a thickness of 250 nm. The simulation results are presented in Fig. 6. It is worth noting that the slight discrepancies between the simulated and theoretical results can be attributed to the interference disruption of the HP plasmon and the energy loss caused by metal absorption.

V. CONCLUSION

In summary, based on the paraxial approximation condition and dispersion relationship in the Drude model, we have researched the unique properties of the HP plasmon, whose propagation trajectory displays an odd symmetric form relative to the focal point. For the superposition of the HP plasmon without any phase offsets, the obtained plasmon exhibited strong self-focusing and self-healing abilities. The

tunable focus intensity of such a plasmon was higher and more concentrated than that of the Pearcey plasmon. Also, the self-healing property was verified by introducing the potential well. This allowed the plasmon to keep the propagation stable in the presence of surface irregularities, and the width of the potential well acted as a modulating factor to reduce the focus intensity. Alternatively, when a π phase offset was introduced, the plasmonic bottle was constructed under the modulation of the chirp factor. By manipulating the chirp factor and dislocation factor, we constructed a kind of multiple plasmonic bottle with tunable number, size, position, and off-axis angle. By filtering a specific spatial spectrum, we found that the self-focusing property and extra foci are controlled by the high-frequency component, explaining the phenomenon that the number of foci is not equal to the number of chirp factors. This discovery is expected to provide an alternative perspective for plasmonic trapping. Ultimately, we confirmed the validity of our results by FDTD numerical simulation.

ACKNOWLEDGMENTS

The authors acknowledge support from National Natural Science Foundation of China (Grants No. 12174122 and No. 11775083), Guangdong provincial Natural Science Foundation of China (Grants No. 2022A1515011482, No. 2022A1515012377, and No. 2024A1515010556), Program of Innovation and Entrepreneurship for Undergraduates (Grant No. 202332020), and Special Funds for the Cultivation of Guangdong College Students' Scientific and Technological Innovation ("Climbing Program" Special Funds) (Grant No. pdjh2024b124).

The authors declare no conflict of interest.

[1] S. Buddhiraju, Y. Shi, A. Song, C. Wojcik, M. Minkov, I. A. D. Williamson, A. Dutt, and S. Fan, Absence of unidirectionally propagating surface plasmon-polaritons at nonreciprocal metal-dielectric interfaces, Nat. Commun. **11**, 674 (2020).

[2] Y. Zhang, C. Min, X. Dou, X. Wang, H. P. Urbach, M. G. Somekh, and X. Yuan, Plasmonic tweezers: For nanoscale optical trapping and beyond, Light: Sci. Appl. **10**, 59 (2021).

[3] X. Liu, J. Gao, J. Gao, H. Yang, X. Wang, T. Wang, Z. Shen, Z. Liu, H. Liu, J. Zhang, Z. Li, Y. Wang, and Q. Li, Microcavity electrodynamics of hybrid surface plasmon polariton modes in high-quality multilayer trench gratings, Light: Sci. Appl. **7**, 14 (2018).

[4] S.-Y. Ding, J. Yi, J.-F. Li, B. Ren, D.-Y. Wu, R. Panneerselvam, and Z.-Q. Tian, Nanostructure-based plasmon-enhanced Raman spectroscopy for surface analysis of materials, Nat. Rev. Mater. **1**, 16021 (2016).

[5] J. Wang, J. Wu, and C. Guo, Abruptly resolving dynamics of acoustic phonons by surface plasmons, Opt. Lett. **32**, 719 (2007).

[6] X. Liu, Z. Huang, C. Zhu, L. Wang, and J. Zang, Out-of-plane designed soft metasurface for tunable surface plasmon polariton, Nano Lett. **18**, 1435 (2018).

[7] W.-Y. Tsai, J.-S. Huang, and C.-B. Huang, Selective trapping or rotation of isotropic dielectric microparticles by optical near field in a plasmonic archimedes spiral, Nano Lett. **14**, 547 (2014).

[8] C. Min, Z. Shen, J. Shen, Y. Zhang, H. Fang, G. Yuan, L. Du, S. Zhu, T. Lei, and X. Yuan, Focused plasmonic trapping of metallic particles, Nat. Commun. **4**, 2891 (2013).

[9] H. Bruhier, J. Dutems, E. Laffont, N. Crespo-Monteiro, I. Verrier, O. Parriaux, P. Berini, and Y. Jourlin, Common-mode plasmon sensing scheme as a high-sensitivity compact SPR sensor, Opt. Lett. **48**, 3733 (2023).

[10] J. Christensen, A. Manjavacas, S. Thongrattanasiri, F. H. L. Koppens, and F. J. García de Abajo, Graphene plasmon waveguiding and hybridization in individual and paired nanoribbons, ACS Nano **6**, 431 (2012).

[11] A. Salandrino and D. N. Christodoulides, Airy plasmon: A nondiffracting surface wave, Opt. Lett. **35**, 2082 (2010).

[12] C. J. Regan, L. Grave de Peralta, and A. A. Bernussi, Two-dimensional Bessel-like surface plasmon-polariton beams, J. Appl. Phys. **112**, 103107 (2012).

[13] Z. Tu, Y. Wu, H. Hu, J. Zhao, H. Tang, Y. Chen, H. Yang, C. Xu, and D. Deng, Airy–Talbot plasmon: An accelerating self-imaging surface wave, Opt. Lett. **47**, 1887 (2022).

[14] Y. Chen, Z. Tu, H. Hu, J. Zhang, Z. Feng, Z. Wang, W. Hong, and D. Deng, Olver plasmon: An accelerating surface wave with various orders, Opt. Lett. **48**, 2030 (2023).

[15] J. D. Ring, J. Lindberg, A. Mourka, M. Mazilu, K. Dholakia, and M. R. Dennis, Auto-focusing and self-healing of Pearcey beams, Opt. Express **20**, 18955 (2012).

[16] M. V. Berry and C. J. Howls, *Digital Library of Mathematical Functions* (National Institute of Standards and Technology, Gaithersburg, 2012), Chap. 36, available at https://dlmf.nist.gov/36.

[17] H. Hu, C. Xu, M. Lin, and D. Deng, Pearcey plasmon: An autofocusing surface wave, Results Phys. **26**, 104416 (2021).

[18] Y. Liu, C. Xu, Z. Lin, Y. Wu, Y. Wu, L. Wu, and D. Deng, Autofocusing and self-healing of symmetric odd-Pearcey Gauss beams, Opt. Lett. **45**, 2957 (2020).

[19] Y. Wu, J. Zhao, Z. Lin, H. Huang, C. Xu, Y. Liu, K. Chen, X. Fu, H. Qiu, H. Liu, G. Wang, X. Yang, D. Deng, and L. Shui, Symmetric Pearcey Gaussian beams, Opt. Lett. **46**, 2461 (2021).

[20] C. Sun, D. Deng, X. Yang, and G. Wang, Propagation dynamics of autofocusing circle Pearcey Gaussian vortex beams in a harmonic potential, Opt. Express **28**, 325 (2020).

[21] A. A. Kovalev, V. V. Kotlyar, S. G. Zaskanov, and A. P. Porfirev, Half Pearcey laser beams, J. Opt. **17**, 035604 (2015).

[22] Y. Yang, Y. Wu, X. Zheng, J. Shi, Y. Luo, J. Huang, and D. Deng, Particle manipulation with twisted circle Pearcey vortex beams, Opt. Lett. **48**, 3535 (2023).

[23] D. Xu, Z. Mo, J. Jiang, H. Huang, Q. Wei, Y. Wu, X. Wang, Z. Liang, H. Yang, H. Chen, H. Huang, H. Liu, D. Deng,

and L. Shui, Guiding particles along arbitrary trajectories by circular Pearcey-like vortex beams, Phys. Rev. A **106**, 013509 (2022).

[24] M. Righini, A. S. Zelenina, C. Girard, and R. Quidant, Parallel and selective trapping in a patterned plasmonic landscape, Nat. Phys. **3**, 477 (2007).

[25] S. Wei, J. Lin, R. Wang, Q. Wang, G. Yuan, L. Du, Y. Wang, X. Luo, M. Hong, C. Min, and X. Yuan, Self-imaging generation of plasmonic void arrays, Opt. Lett. **38**, 2783 (2013).

[26] I. Epstein and A. Arie, Dynamic generation of plasmonic bottle-beams with controlled shape, Opt. Lett. **39**, 3165 (2014).

[27] W. L. Barnes, A. Dereux, and T. W. Ebbesen, Surface plasmon subwavelength optics, Nature (London) **424**, 824 (2003).

[28] S. A. Maier, *Plasmonics: Fundamentals and Applications* (Springer, New York, 2007).

[29] T.-C. Poon and T. Kim, *Engineering Optics with MATLAB®* (World Scientific, Singapore, 2017).

[30] P. Genevet, J. Dellinger, R. Blanchard, A. She, M. Petit, B. Cluzel, M. A. Kats, F. de Fornel, and F. Capasso, Generation of two-dimensional plasmonic bottle beams, Opt. Express **21**, 10295 (2013).

[31] L. Yin, V. K. Vlasko-Vlasov, J. Pearson, J. M. Hiller, J. Hua, U. Welp, D. E. Brown, and C. W. Kimball, Subwavelength focusing and guiding of surface plasmons, Nano Lett. **5**, 1399 (2005).

[32] Z. Mo, J. Jiang, Q. Wei, D. Xu, H. Yang, H. Huang, Y. Wu, H. Liu, L. Shui, and D. Deng, Multiple and off-axis optical bottles from the chirped circular Pearcey Gaussian vortex beams, Opt. Express **30**, 1762 (2022).

[33] S. Wang, C. Zhao, and X. Li, Dynamical manipulation of surface plasmon polaritons, Appl. Sci. **9**, 3297 (2019).

[34] S.-H. Chang, S. K. Gray, and G. C. Schatz, Surface plasmon generation and light transmission by isolated nanoholes and arrays of nanoholes in thin metal films, Opt. Express **13**, 3150 (2005).

[35] J. Lin, J. P. B. Mueller, Q. Wang, G. Yuan, N. Antoniou, X.-C. Yuan, and F. Capasso, Polarization-controlled tunable directional coupling of surface plasmon polaritons, Science **340**, 331 (2013).

[36] P. Zhang, S. Wang, Y. Liu, X. Yin, C. Lu, Z. Chen, and X. Zhang, Plasmonic Airy beams with dynamically controlled trajectories, Opt. Lett. **36**, 3191 (2011).